GT2018-77071

ON THE INTERACTIONS OF A ROTOR BLADE TIP FLOW WITH AXIAL CASING GROOVES IN AN AXIAL COMPRESSOR NEAR THE BEST EFFICIENCY POINT

Huang Chen	**Yuanchao Li**	**Joseph Katz**
Johns Hopkins University	Johns Hopkins University	Johns Hopkins University
Department of Mechanical Engineering	Department of Mechanical Engineering	Department of Mechanical Engineering
Baltimore, MD, USA	Baltimore, MD, USA	Baltimore, MD, USA

ABSTRACT

Previous studies have shown that axial casing grooves (ACGs) are effective in delaying the onset of stall, but degrade the performance of axial turbomachines around the best efficiency point (BEP). Our recent experimental study [1] in the JHU refractive index-matched liquid facility have examined the effects of ACGs on delaying stall of a one and half stage compressor. The semicircular ACGs based on Müller et al. [2] reduce the stall flow rate by 40% with a slight decrease in pressure rise at higher flow rates. Stereo-PIV (SPIV) measurements at a flow rate corresponding to the pre-stall condition of the untreated machine have identified three flow features that contribute to the delay in stall. Efficiency measurements conducted as part of the present study show that the ACGs cause a 2.4% peak efficiency loss. They are followed by detailed characterizations of the impact of the ACGs on the flow structure and turbulence in the tip region at high flow rates away from stall. Comparisons with the flow structure without casing grooves and at low flow rate are aimed at exploring relevant flow features that might be associated with the reduced efficiency. The SPIV measurements in several meridional and radial planes show that the periodic inflow into the groove peaks when the rotor blade pressure side (PS) overlaps with the downstream end of the groove, but diminishes when this end faces the blade suction side (SS). The inflow velocity magnitude is substantially lower than that occurring at a flow rate corresponding to the pre-stall conditions of the untreated machine. Yet, entrainment of the PS boundary layer and its vorticity during the inflow phase generates counter-rotating radial vortices at the entrance to the groove, and a "discontinuity" in the appearance of the tip leakage vortex (TLV). While being exposed to the blade SS, the backward tip leakage flow causes flow separation and formation of a counter-rotating vortex at the downstream corner of the groove, which migrates towards the passage with increasing flow rate. Interactions of this corner vortex with the TLV cause

fragmentation of the latter, creating a broad area with secondary flows and elevated turbulence level. Consequently, the vorticity shed from the blade tip remains scattered from the groove corner to the blade tip long after the blade clears this groove. The turbulence peaks around the corner vortex, the TLV, and the shear layer connecting it to the SS corner. During periods of inflow, there is a weak outflow from the upstream end of the groove. At other phases, most of the high secondary flows are confined to the downstream corner, leaving only weak internal circulation in the rest of the groove, but with a growing shear layer with elevated (but weak) turbulence originating from the upstream corner. Compared to a smooth endwall, the groove also increases the flow angle near the blade tip leading edge (LE) and varies it periodically. Accordingly, the magnitude of circulation shed from the blade tip and leakage flow increase near the leading edge. The insight from these observations might guide the development of ACGs that take advantage of the effective stall suppression by the ACGs but alleviate the adverse effects at high flowrates.

INTRODUCTION

Many studies, e.g. [3–8], have shown that casing treatments, especially axial casing grooves, are effective in delaying the onset of stall. However, they tend to cause efficiency loss at higher flow rate, near the best efficiency point (BEP) of the machine. Measurements by Fujita and Takata [9] show a positive linear relationship of the stall margin improvement with the efficiency penalty. Experimental studies by Müller et al. [2] have shown that ACGs similar to those used in the present paper cause a 0.5% efficiency penalty in a transonic compressor rotor. Reynolds-averaged Naiver-Stokes simulations by Wilke and Kau [10] show that when the ACGs are located around a transonic rotor blade LE, there is a 0.2% efficiency loss, but the loss increases to 4% when the groove is centered above the rotor. They associate the efficiency loss

with the distortion of shock system in the blade passage. Similar trends have been reported in [4,11], suggesting that positioning the grooves around the LE minimizes the efficiency loss while maintaining similar stall margin improvements compared with the grooves located at the mid-chord. In contrast, results reported by Beheshti et al. [12] based on Favre-averaged Naiver-Stokes simulations have shown an increase in the peak efficiency by ACGs. Efforts have also been invested in modifying groove geometry to minimize the efficiency loss. For example, Weichert et al. [13] propose a self-regulating casing treatment that maintains the circulation in the groove at low flow rate to delay stall, but minimizes flow into the groove at high flow rate to improve the efficiency. They achieve a 6% increase in stall margin and 0.8% efficiency loss.

In spite of their significance, there are very few experimental studies that resolve the interactions of tip flow with ACGs, in great part due to the challenging task of measuring the flow in the confined rotor tip region. To address this access problem, in the JHU facility the refractive index of the acrylic blades and casing are matched with that of the fluid, an aqueous sodium iodide solution. This approach provides unobstructed optical access to the blade tip region, but is limited to incompressible flows. Relevant previous work performed in this facility has resolved the flow structure in the rotor blade tip region, including in the tip gap [14–18]. Velocity, vorticity and turbulence data for the present machine without grooves have been included in previous publications [19–22], including detailed characterization of the mechanisms leading to the onset of stall. A recent study using ACGs skewed by 45° and partially overlapping with the blade LE, following Müller et al. [2], has focused on the stall delaying mechanism at low flow rate [1]. Three contributing flow features have been identified, including suction of the TLV into the groove, as well as periodic modification to the flow angle and the circumferential velocity near the rotor blade leading edge.

The present study expands these efforts by emphasizing on the interactions of the tip flow with ACGs at/near the BEP. Our main objective is to identify mechanisms that contribute to the loss of efficiency at high flow rates. The previously observed 40% reduction in stall flow rate, but slight pressure rise degradations at high flow rates [1] are supported by efficiency measurements showing that the ACGs cause a 2.4% peak efficiency loss, but substantial improvements at lower flow rate. The flow is characterized using qualitative flow visualization by cavitation, and quantitative SPIV measurements. The results are compared with those obtained at lower flow rate and in the same machine with a smooth endwall. Unlike the observations at low flow rate, where most of the TLV is entrained into the groove, near the BEP, substantial fractions of the TLV escape and develop downstream to the groove. Yet, periodic interactions of the blade and tip leakage flow with the grooves cause "discontinuities" in the TLV trajectory, and formation of a counter-rotating corner separation vortex near the downstream corner of the groove, which fragments the TLV and is a major generator of turbulence. The grooves also increase the inflow angle near the blade LE and modify the blade load distribution.

NOMENCLATURE

A_T = through flow area
c = rotor blade tip chord
h = width of the rotor blade tip gap
H = rotor blade span
k = turbulent kinetic energy
L = nominal distance from the hub to the inner casing endwall
p_{exit} = static pressure at stator outlet
p_{in} = static pressure at IGV inlet
Q = volumetric flow rate
r, z, θ = radial, axial and circumferential coordinates
r^* = Normalized radial coordinate
s = rotor blade chordwise coordinate
T = motor input torque
u_r, u_z, u_θ = radial, axial and circumferential velocity
U_T = rotor blade tip speed
U_n^* = tip leakage flow normal to the blade chord in the rotor reference frame
u' = velocity fluctuation
V_z = average axial velocity in the rotor passage
ρ = NaI solution density
φ = flow coefficient
ψ_{SS} = static-to-static pressure rise coefficient
ω_r, ω_θ = radial and circumferential vorticity
Ω = rotor angular velocity
$< >$ = ensemble-averaged quantity

Table 1 Stage relevant geometrical parameters

Casing diameter (D) (mm)	457.2
Hub radius (r_{hub}) (mm)	182.9
Rotor passage height (L) (mm)	45.7
Rotor diameter (D_R) (mm)	453.6
Rotor blade chord (c) (mm)	102.6
Rotor blade span (H) (mm)	43.9
Rotor blade stagger angle (γ) (deg)	58.6
Rotor blade axial chord (c_A) (mm)	53.5
Measured tip clearance (h) (mm)	1.8 (0.0175c or 0.041H)
Axial casing groove diameter (mm)	34.8
Groove skew angle (deg)	45
Total number of grooves	60
Shaft speed (Ω) (rad s^{-1}) {RPM}	50.27 {480}
Rotor blade tip speed (U_T) (m s^{-1})	11.47
Reynolds number ($U_T c / v$)	1.07×10^6

EXPERIMENTAL SETUP

The one-and-half stages compressor has a 20-blade inlet guide vane (IGV), a 15-blade rotor and a 20-blade stator (Fig.1a), with blade geometries based on the low-speed axial compressor (LSAC) facility at NASA Glenn [16,23]. Detailed descriptions of the compressor can be found in [21,22] for a smooth endwall, and in [1] for the same system containing ACGs. Table 1 shows relevant geometrical parameters of this machine. The working fluid is a 62%-63% by weight aqueous sodium iodide solution, whose refractive index matches that of the acrylic casing and rotor blades. The kinematic viscosity of the solution is around 1.1×10^{-6} m^{2}s^{-1} [24] and its specific gravity is about 1.8. Following Müller et al. [2], as shown in Fig.1 b&c, the semi-circular grooves have a diameter of 34.8mm (65% C_A), of which 33% overlap with the rotor, and the rest extend upstream of the rotor. The four-per-passage grooves are evenly spaced and skewed by 45° towards the rotation direction of the rotor (Fig.1c). The grooves are machined in an acrylic ring and then installed around the rotor. The directly measured tip clearance in the sample area is 1.8mm, i.e. 3.4% of the axial chord, and 4.1% of the blade span.
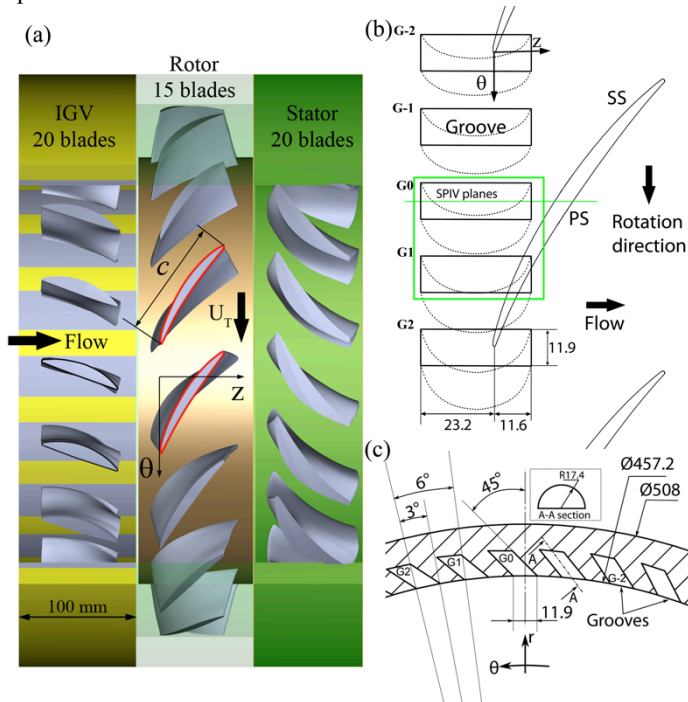
Figure 1: (a) Configuration of the one and a half stages compressor. (b and c) The ACG configurations. All dimensions are in mm.

The compressor is installed in the JHU closed-loop refractive index-matched facility, whose detailed description is provided in [14–16]. The rotor is driven by a precision-controlled AC motor whose speed is fixed at 480 RPM during current experiments. A 20 HP auxiliary pump has been added

to the other side of the loop, allowing us to operate the compressor at higher flow rate than before. Based on the tip speed of the rotor and chord length, the Reynolds number is 1.07×10^6. The rotor blade phase is monitored by a shaft encoder, enabling us to perform synchronized measurements at desired phases. A strain gauge based torque meter (SensorData® T261-STD-A) integrated with the shaft before it penetrates the loop is used for measuring the power input to the machine. This sensor has been calibrated by the manufacturer prior to the experiments, and they claim that the specified uncertainty is in the order of 0.1% for the present conditions. The torque required to overcome the resistance of the bearing system and rotor hub has been measured by running the rotor hub with flush blanks replacing the rotor blades under the same conditions as the experiments. This torque is subtracted from the measured values when the torque applied on the blades is calculated. The static pressure difference across the machine is monitored by a differential pressure transducer connected to pressure ports upstream of the IGV and downstream of the stator [16,21]. The volumetric flow rate is measured by integrating the velocity profile obtained from translating a Pitot tube in the radial direction in the return line of the loop. The data for each point in the performance curve is recorded after operating the machine for several minutes under the same conditions. Accounting for all the contributors, the uncertainties associated with measured head rise, flow rate and efficiency are around 1.2%, 1.7% and 2.2%, respectively. The uncertainty in efficiency includes effects of measurements of flow rate, pressure rise, torque, and even speed (small). The uncertainty in pressure coefficient (1.2%) accounts for the transducer's accuracy and standard deviation of results integrated to a single averaged value (200,000 data points). The uncertainty in flow coefficient (1.7%) includes effect of transducer accuracy, Pitot tube location and standard deviation of variations in data. The uncertainty in torque (very small) includes effects of all the sensors, subtraction of the torque without blades, and speed. The flowrate and pressure rise are the main contributors to the uncertainty in efficiency.

The facility is equipped with a half-filled tank located above the loop to control the mean pressure. Cavitation induced at low-pressure conditions is used to visualize vortical structures in the rotor passage. During these visualization tests, the flow field is illuminated by halogen lamps and images are recorded by high speed cameras. During SPIV measurements, the pressure is increased and kept high to suppress all kinds of cavitation.

The SPIV setups for measurements in meridional and nearly radial (z, θ) planes are shown in Fig. 2. To satisfy the imaging conditions, the lenses are tilted by the Scheimpflug angles relative to the imaging arrays, with their axes are aligned perpendicularly to the acrylic prism surfaces. The beam of a dual head, 200mJ/pulse Nd:YAG laser is expanded to a 1mm

thick laser sheet to illuminate the flow field, which is seeded with 13μm, silver coated hollow glass particles. As discussed in [25], these particles have a specific gravity of 1.6, i.e. slightly less than the fluid, but they are expected to follow the flow for the present conditions. The delay between exposures is fixed at 20μs. As shown in Fig. 2a, in most the present meridional plane measurements, the laser sheet is cutting through the center of the groove marked as G0 at the inner surface of the casing endwall. In sample data aimed at elucidating certain trends, we also provide results for the meridional plane aligned with θ =1.5°, which nearly intersects with the forward end of the groove. In Fig. 1b, grooves located in the positive circumferential direction are named G1, G2, etc., while those located to the other direction are named G-1, G-2, etc. The particle images are recorded by a pair of Imperx B6640 CCD cameras (6600×4400 pixels) using a field of view of 46.3×42.6 mm^2. Data have been acquired at two different axial locations, covering most part of the blade passage. In Fig. 2b, a pair of 2048×2048 pixels PCO 2000 cameras is used to record data in two planes that are aligned perpendicularly to the radial direction in the middle of the G0 groove. Since these planes are flat, their distance from the endwall decreases with increasing θ. When the blade span is vertical, plane R1 intersects with the blade tip at $r* = 0.96$, and plane R2 cross the radius in the tip gap at $r* = 0.98$. Here, $r*$ is the normalized radial coordinate, defined as $r*=(r-r_{hub})/L$, where L is the distance between the hub and the casing endwall. The field of view is 47.9×52.43 mm^2, covering both G0 and G1, as shown in Fig. 1b. Note that due to the casing curvature, planes R1 and R2 are located close to the entrance to groove G1, where they are no longer aligned in the radial direction. SPIV data have been recorded at two flowrates, φ=0.35 and 0.38, with the latter, as shown later, corresponding to BEP of the untreated machine. Here, $\varphi=V_Z/U_T$, where is V_Z is the spatially averaged axial velocity in the rotor passage and U_T is the tip speed. We also have previously obtained data for φ=0.25 [1,22], which corresponds to pre-stall conditions of the untreated machine. Calibration of the SPIV system consists of a two-step process, following Wieneke [26]. The first step is performed by lifting the entire imaging system vertically to record images of a dotted target translated in a box filled with the same working fluid. In the second, fine self-calibration phase, the system is lowered back to record and correlate images of particles located in the actual sample area [26]. Further details can be found in [20–22]. Image preprocessing includes background removal and application of a modified histogram equalization algorithm described in [27]. The vector maps are calculated by a multi-pass FFT-based cross-correlation commercial software LaVison DaVis®. Post-processing consists of application of a universal outlier detection algorithm [28] to reject spurious vectors. With 50% overlap, the final interrogation window size is 32×32 pixels for the meridional planes, and 24×24 pixels for the (z, θ) planes, resulting vector spacing of 0.142mm and 0.251mm, respectively. Our previous studies [15] have shown that the uncertainties in instantaneous velocities are around 0.4~0.8%U_T, as long as there are at least 5 particles in each interrogation window. The ensemble-averaged results are expected to have an order of magnitude lower uncertainty.

In this paper, data will be presented in the cylindrical coordinate system (r, θ, z) centered at the compressor center. The corresponding instantaneous velocity components are $(u_r, u_\theta, u_z,)$. Unless specified, the velocity components are all presented in the lab reference frame. Ensemble-averaged components $(U_r, U_\theta, U_z,)$ are obtained by averaging at least 1000 realizations recorded under the same blade orientation and flow conditions. More than 1500 realizations of the velocity fluctuations, defined as $u_i' = u_i-U_i$, are used for calculating the statistics of turbulence parameters. The blade orientation/phase is represented by the blade chord fraction (s/c), which indicates the point where the meridional plane laser sheet (at G0 center) cuts the blade chord. Data have been recorded at 14 blade phases covering an entire blade passage for each setup and each flow rate.
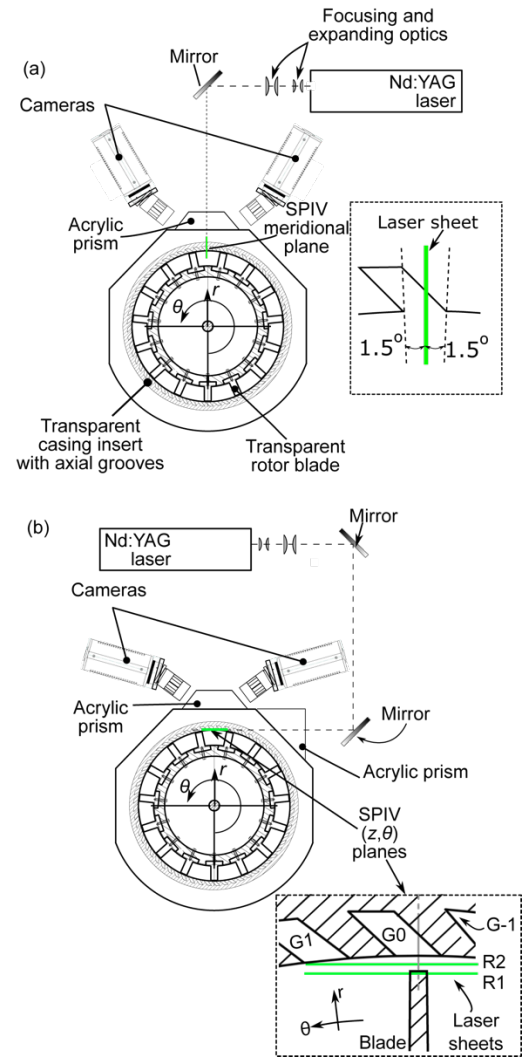
Figure 2: Experimental setups for (a) SPIV in meridional planes, and (b) SPIV in (z, θ) planes.

RESULTS AND DISCUSSIONS

Performance and efficiency

Figure 3 compares the performances of the machine with and without ACGs. The static-to-static head rise coefficient is defined as $\psi_{SS}=(P_{exit}-P_{in})/0.5\rho U_T^2$, where $P_{exit}-P_{in}$ represents the pressure rise across the entire machine. The efficiency of the machine is calculated from $\eta=(P_{exit}-P_{in})Q/T\Omega$, where Q is the volumetric flow rate and T is the torque measured after subtracting the effects of bearings. They are both plotted against the flow coefficient, $\varphi=V_Z/U_T$, where $V_Z= Q/A_T$ and A_T being the through-flow area. Figure 3a shows that the stall onset flow coefficient decreases from $\varphi=0.25$ without grooves to $\varphi<0.15$ when ACGs are installed. The most prominent mechanism causing the onset of stall in untreated endwall involves formation of backflow vortices (BFVs) that propagate from the SS of one blade to the leading edge of the next blade. The origin of the BFVs is described in [21]. Installation of the grooves, as discussed in [1], has three primary effects, namely suction of the TLV into the groove, periodic modifications to the flow angle (leading edge loading), and reduction in the circumferential velocity near the leading edge of the blade, which suppresses the formation of the BFVs.

However, at $\varphi>0.36$, the grooves cause a slight decrease in ψ_{SS}. Figure 3b shows that the BEP for the untreated machine is $\varphi=0.38$, where $\eta=0.84$. Adding the grooves causes a 2.4% decrease in efficiency at $\varphi=0.38$, and shifts the BEP to $\varphi\sim0.36$. The lower efficiency at $\varphi=0.38$ is associated with both a lower head rise and a higher torque. The efficiency of the two cases is almost the same at $\varphi=0.35$. At lower flow rates, the grooves cause a slight increase in efficiency, indicating that the dramatic improvements in pressure rise co-occur with a similar increase in torque.

The flow visualizations and velocity measurements have been performed at three different flow rates: $\varphi=0.25$ which corresponds to the pre-stall condition of the machine without casing groove; $\varphi=0.35$ when the two cases have similar efficiency but the head rise coefficient is higher for the grooved case; and $\varphi=0.38$ which is the BEP for the untreated rotor. The reason for focusing on $\varphi=0.35$ is the previously obtained vast database on the flow structure and turbulence without grooves under the same condition.

Flow visualization of vortical structures by cavitation

Figures. 4a and b present two sample cavitation images at two blade phases at $\varphi=0.35$, which are aimed at highlighting the interactions of the tip region vortical structures with ACGs. In both cases, the TLV has multiple kinks. In Fig. 4a, which corresponds to $s/c=0.33$, the blade mid chord overlaps with the G0 groove corner, and the LE passes above the G1 groove. The TLV initially rolls up between G0 and G1, as indicated by the tip leakage cavitation, which indicates strong tip leakage flow [16], and the thin vortical filament aligned the blade SS. The insert in Fig. 4a shows that part of a vortical structure originating from the PS is entrained into the G0 groove corner. As shown later, this entrainment is caused by an intermittent radial jet that peaks when the downstream end of the groove is

exposed to the pressure side of the blade. Similar entrainment of vorticity originating from the PS have been observed at $\varphi=0.25$ [1]. Further along the SS, the TLV appears to be aligned with the downstream end of the G0 groove, even beyond the this groove, but then starts meandering as it begins to interact with the G-1 groove. Fig. 4b shows a different phase, corresponding to $s/c=0.55$. The presence of multiple structures and a discontinuity in the TLV trajectory appear to develop near the G0 groove corner. In particular, a pair of vortical structures appears to be aligned with the downstream end of this groove. The SPIV data presented later in this paper indicate that these structures correspond to a pair of counter-rotating vortices, the downstream one being part of the TLV, and the upstream one being a separation vortex at the groove corner. As a comparison, Fig. 4c shows the TLV at $\varphi=0.38$, where the noticeable leakage flow and TLV rollup occur at higher s/c compared to the images at $\varphi=0.35$, and substantial fractions of the TLV develops downstream of the grooves. Yet, the TLV is still parallel initially to the edge of the G0 groove, but then has a kink before it reaches the G-1 groove.

SPIV measurements in meridional planes

Ensemble-averaged circumferential vorticity distributions and vectors of in-plane velocity components (U_z, U_r) in the center meridional plane of G0, at four different phases, and at $\varphi=0.35$, with and without casing grooves, are shown in Fig. 5. The fields of view in Fig. 5a-d are expanded by patching results

(a)

(b)
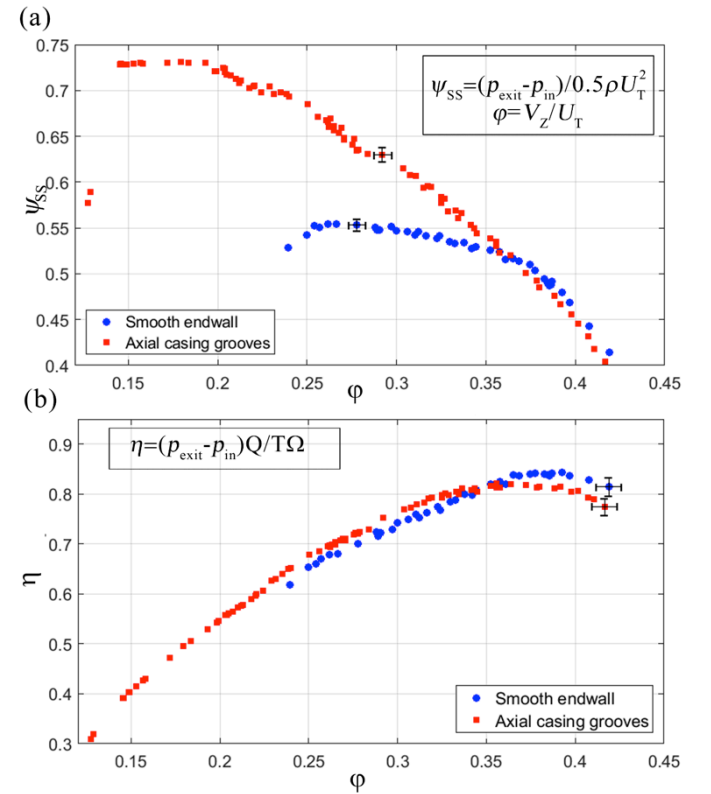
Figure 3: Performance curves with and without the axial casing grooves. (a) Static head rise and (b) efficiency.
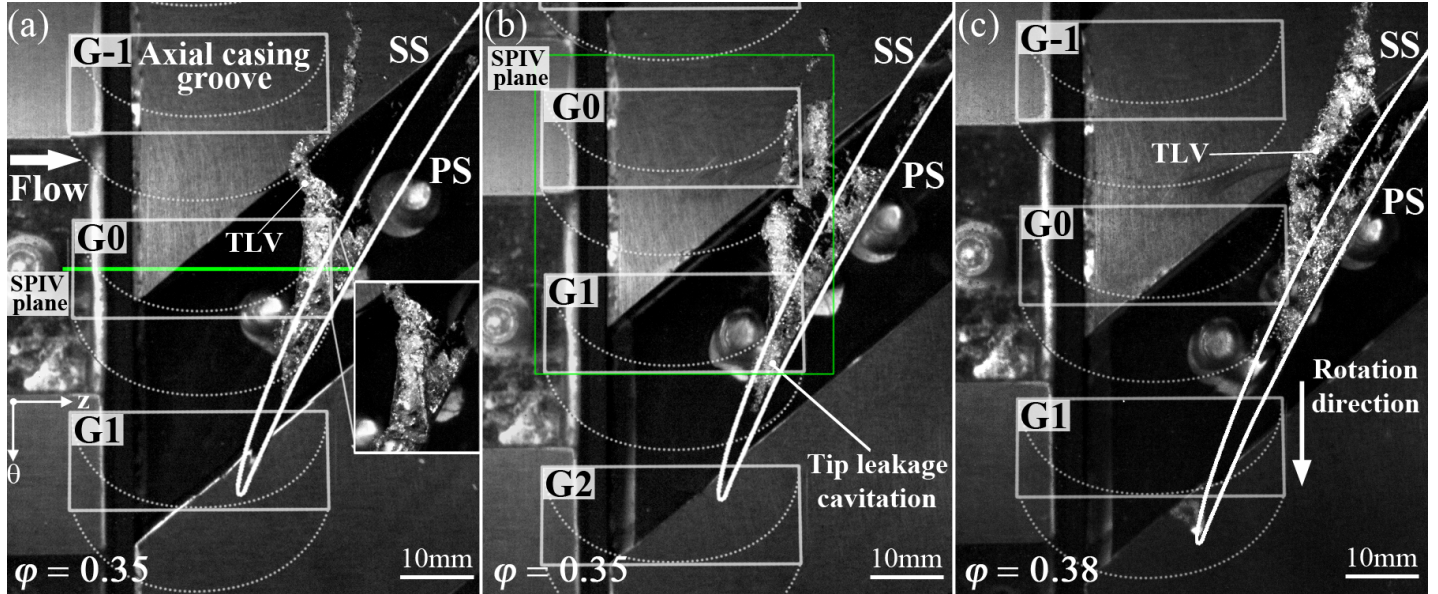
Figure 4: Sample cavitation images showing vortical structures in the rotor passage with ACG (a and b) at φ=0.35 for two different blade phases, and (c) at φ=0.38. Entrances to the grooves are indicated by solid white lines, and their outlines are marked by dashed lines.

obtained at two different axial locations. In Fig. 5a, the blade PS is aligned slightly ahead of the downstream corner of the groove, resulting in generation of a rapid radial jet straight from the PS into the groove. This jet presumably carries with it part of the PS boundary layer vorticity, which appears to be distributed along the blade tip and to a lower extent in the SS. A distinct TLV has not formed yet, similar to the corresponding smooth endwall trend shown in Fig. 5e. The velocity magnitude of the outflow from the groove at $-0.4<z/c_A<-0.15$ is much lower than that in the inflow jet. Upstream of the blade, a broad shear layer containing relatively low positive vorticity is aligned parallel to the endwall and extends from the groove upstream corner to the vicinity of the blade SS. Another region with elevated vorticity and a circulating flow pattern appears downstream of the PS, starting from z/c_A=0.4. This region contains vorticity associated with the tip vortex of the previous blade passage. The broad region is caused by TLV breakup, as discussed in several of our previous papers [16,20,21].

At s/c=0.33 shown in Fig. 5b, the blade tip is located under the downstream corner of the groove, at nearly the same orientation relative to the G0 groove in Fig. 4a. Vorticity originated from the blade PS is carried in part into the groove by the still strong jet, and the rest is entrained into the SS as the TLV starts rolling up. A negative vortex containing the endwall boundary layer vorticity begins to develop as the tip leakage flow separates at the downstream corner of the groove. We refer to this structure as a corner vortex in subsequent discussions. In contrast, Fig. 5f shows that a distinct TLV is already formed near the blade tip SS corner for the smooth endwall.

In Fig. 5c, at s/c=0.55, when the blade SS is located downstream of the groove. This phase is similar to that of the flow relative to G0 groove in Fig. 4b. Here, the negative corner vortex grows into a large structure, which is centered radially inward from the endwall, i.e. it occupies part of the main flow passage. It forms a counter-rotating vortex pair with the TLV, which presumably corresponds to the parallel structures located on both sides of the corner evident in the cavitation image shown in Fig. 4b. Interactions of the corner vortex with the TLV appear to have several effects. First, flow induced by the TLV is likely to be the cause for the radial inward migration of the corner vortex. Second, flow induced by the corner vortex broadens the area occupied by the ensemble-averaged TLV. Accordingly, the associated peak vorticity is substantially lower than that measured near the smooth endwall (Fig. 5g) in spite of the higher overall circulation near the grooved endwall (data will follow). To elucidate some of the processes involved, Fig. 6 provides an instantaneous sample at the same phase, showing that the TLV is fragmented with some of its parts forced to remain near the groove corner by flow induced by the corner vortex. Third, at this phase, the rapid jet into the groove is diminished, and the flow around the downstream corner of the groove is driven mainly by corner vortex. Consequently, there is radial inflow into the groove at $0.1<z/c_A<0.15$, and a negative radial velocity (outflow) near the corner. The velocity in the rest of the groove is much lower implying that most of the tip-groove interactions are concentrated at the downstream corner. In addition, Figs. 5c and d display additional notable trends. First, there is a low-speed radial flow into the groove near its upstream end, at $z/c_A\sim-0.43$, which exits from the groove well upstream of the blade, around z/C_A=-0.3. Hence, the associated shear layer becomes wavy. Second, downstream of the blade, a circular flow with elevated vorticity, which is associated with the TLV of the previous blade, has already reached the PS of the blade.
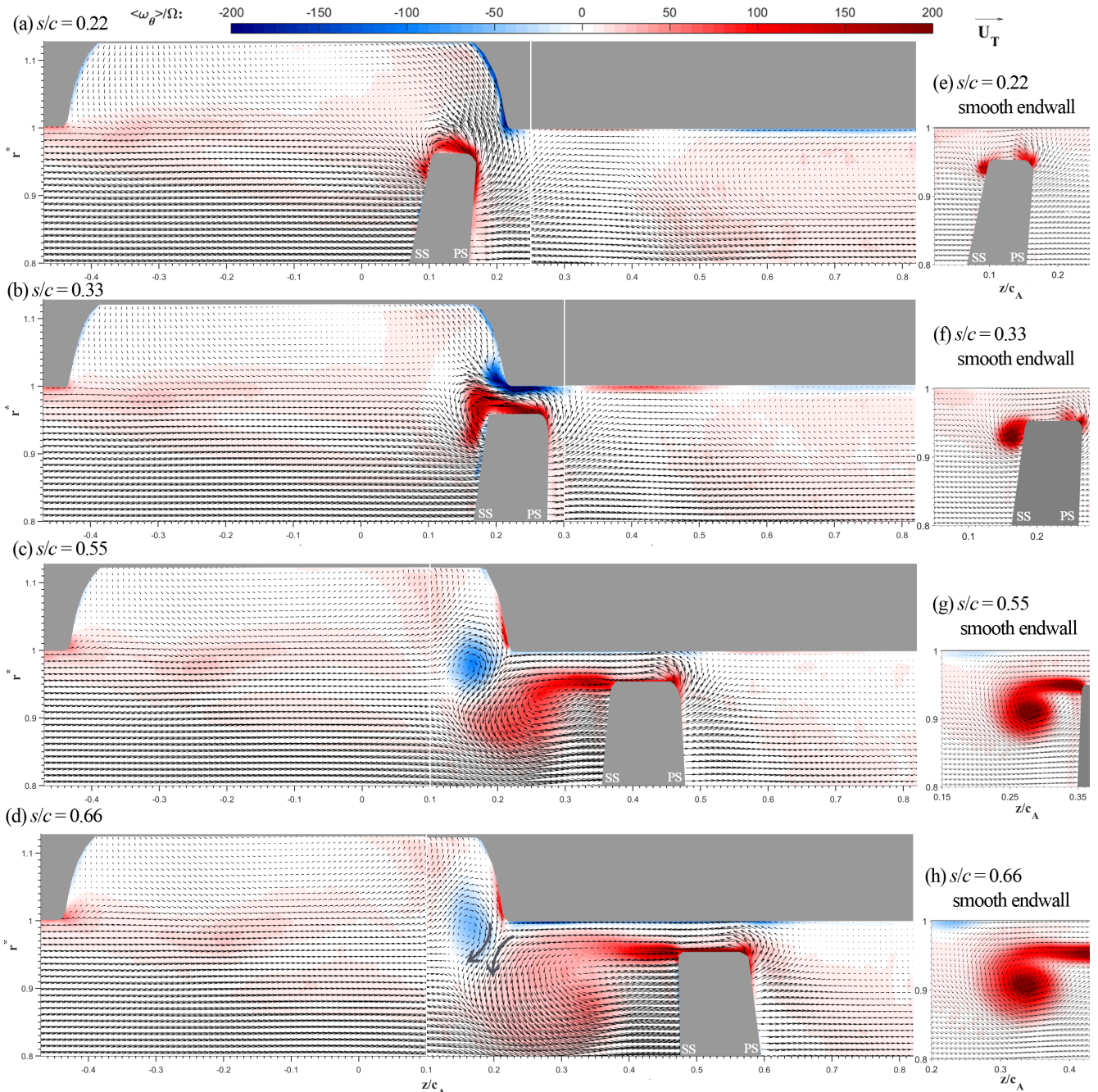
Figure 5: Ensemble-averaged vorticity ($<\omega_\theta>/\Omega$) distributions superimposed on vectors of (U_z, U_r) in meridional planes with casing grooves (left column) and a smooth endwall (right column) at φ=0.35. The chord wise locations are indicated above each plot along with a reference vector showing U_T. Arrows in (d) highlight the counter-rotating vortex pair. Vectors are diluted by 3:1 in both directions for clarity.

At s/c=0.66, Fig. 5d shows that the blade section aligned with the sample meridional plane is already located "far" downstream of the groove. Yet, the counter-rotating vortex pair persists, but with a lower peak vorticity. The area containing positive vorticity associated with the TLV is larger than that observed in at lower s/c, and much larger than the size of the TLV of the smooth endwall (Fig. 5h), where the TLV is still compact and has a higher peak vorticity. The axial extent of the huge area covered by positive vorticity associated with the TLV still starts near the groove corner, while the center of swirl moves downstream. The radial extent of this region also expands to r^*<0.8. Yet, the inflow and outflow around the downstream corner of the groove is still dominated by the corner vortex.
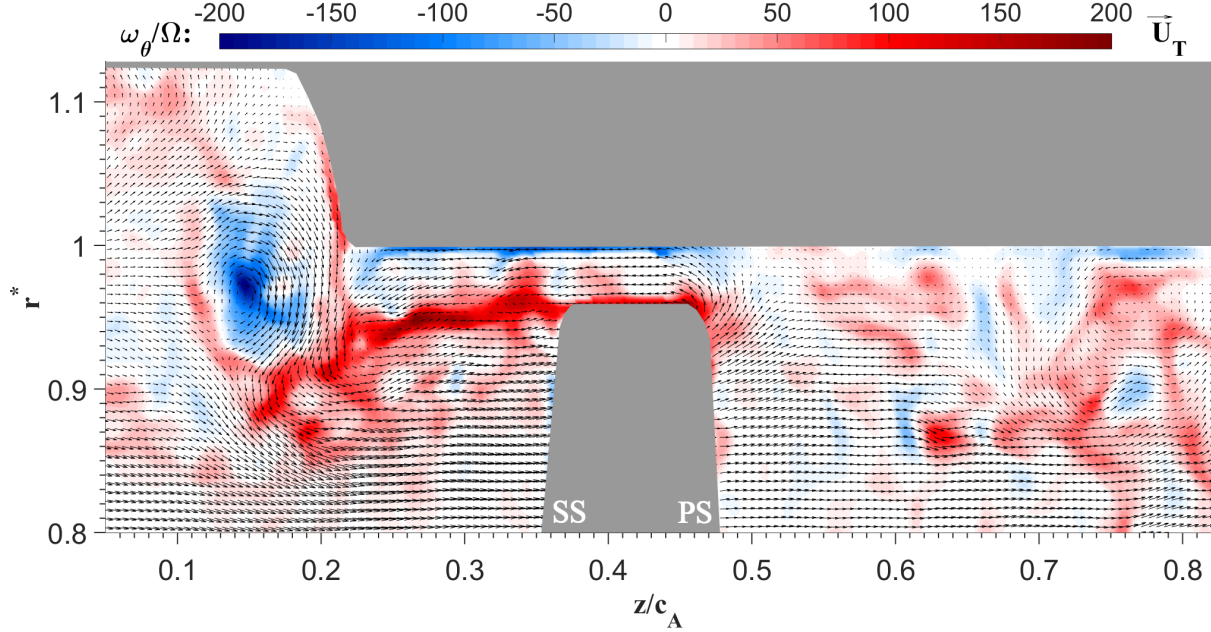
Figure 6: A sample instantaneous vorticity (ω_θ/Ω) and (U_z, U_r) distributions in the downstream meridional plane for s/c=0.55 and φ=0.35. Vectors are diluted by 2:1 in both directions.

To demonstrate the influence of flow rate on the flow around the groove corner, Fig. 7 compares the flow fields at φ=0.25, 0.35 and 0.38, all at s/c=0.44. At φ=0.25 (Fig. 7a), there is still a strong inflow into the groove in the downstream end, and an outflow at the upstream end, which extends deeper into the passage. Accordingly, the entire corner vortex is located inside the groove, and there is no radial outflow at the downstream end. This fast inflow entrains part of the blade circulation into the groove, preventing it from being rolled up into the TLV. Consequently, the TLV circulation starts to decrease starting at mid-chord [1]. Additional data for this flow rate at other phases can be found in [21]. The distributions of $<\omega_\theta>$ at φ=0.35 and 0.38 (Figs. 7b and c, respectively) contain a corner vortex and a radial outflow at the downstream corner, but the size and strength of this structure decrease with increasing flow rate. Furthermore, consistent with the delayed TLV rollup and leakage flow observed in the cavitation images, the TLV strength and area also decrease with increasing flow rate, at least up to s/c=0.44. In the upstream end of the groove, the direction flow changes from a strong outflow in the upstream at φ=0.25 to a weak inflow into the groove at φ=0.35, which increases slightly at φ=0.38 (discussion follows). Finally, the shift in the location of the corner vortex with increasing flow rate impacts the flow at higher chord fractions as well. In particular, Fig. 8 shows that for φ=0.38 and at s/c=0.66, the negative corner vortex is already located within the passage. In contrast, at φ=0.35 and the same location, Fig. 5d shows that only the bottom half of this structure is inside the main passage. At even higher s/c (not shown), the clear elevated negative vorticity region upstream of the TLV persists at φ=0.38 all the way to the trailing edge of the blade. Conversely, a diminishing signature of this corner vortex remains latched to the groove

corner at φ=0.35. It is worth noting that for the smooth endwall and present tip gap, the negative vorticity originating from the endwall boundary layer remains near the casing, and is not entrained away from the wall by the TLV (Figs. 5g &h, [22]).

SPIV measurement results – (z, θ) planes

Figure. 9 provides color contours of U_r and $<\omega_r>$ and vectors of (U_θ, U_z) in the *(z, θ)* planes located at r^*=0.96 and 0.98 (see Fig. 2b), all for s/c=0.33 and φ=0.35. This phase corresponds to those in Figs. 4a&5b. The r^*=0.96 plane in Fig. 9a nearly coincides with the blade tip. The positive U_r along most of the blade PS indicates radial flow into the tip gap. The elevated U_r in the PS area coinciding with the G1 groove represents inflow into the groove. The r^*=0.98 plane coinciding with the tip gap shown in Fig. 9b displays a strong radial inflow jetting into the G0 groove in the high θ (high y/L) edge of the downstream corner, where the blade PS is located just beyond the groove. It also shows radial inflow into the G1. The outflow from both grooves, with negative U_r, is concentrated near the high θ region of the upstream corners. The sharp transition in the sign of U_r along the blade SS in Fig. 9a is induced by the TLV, and can be used to identify its trajectory. Similar to the cavitation image in Fig. 4a, the TLV has a kink at the high θ corner of the G0 groove, at the same location as the strong radial inflow into the groove (Fig. 9b). The negative U_r upstream of the radial jet is induced by the TLV, which at this phase is located above the blade tip, consistent with the $<\omega_\theta>$ distributions presented in Fig. 5b. The radial vorticity distributions in the tip gap (r^*=0.98, Fig. 9d) show that the jet is bounded by a pair of counter-rotating vortices, but there is no sign for this vortices at r^*=0.96 (Fig. 9c). This phenomenon is
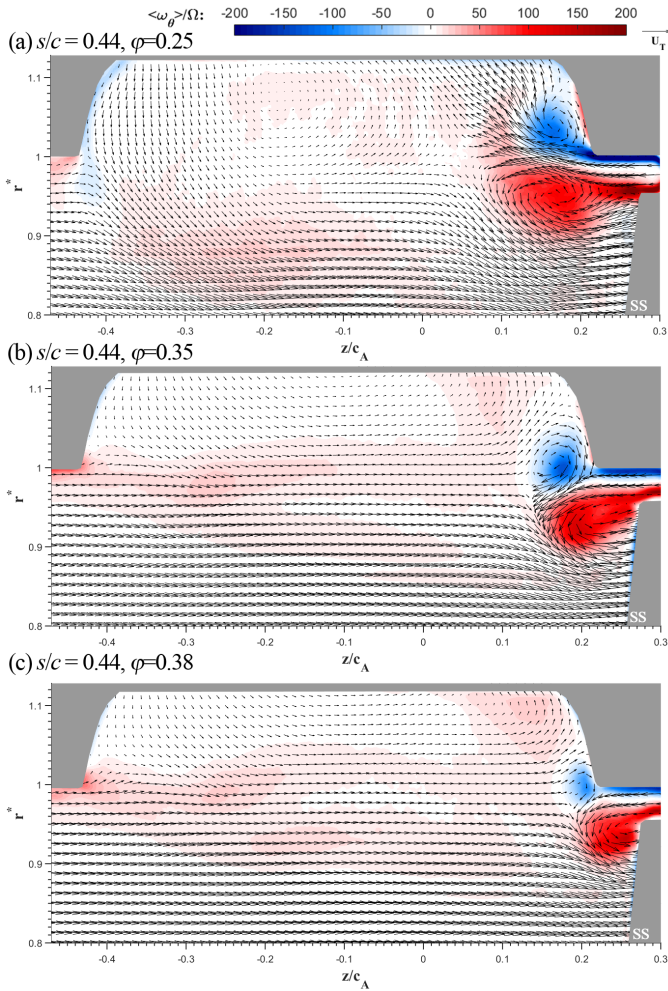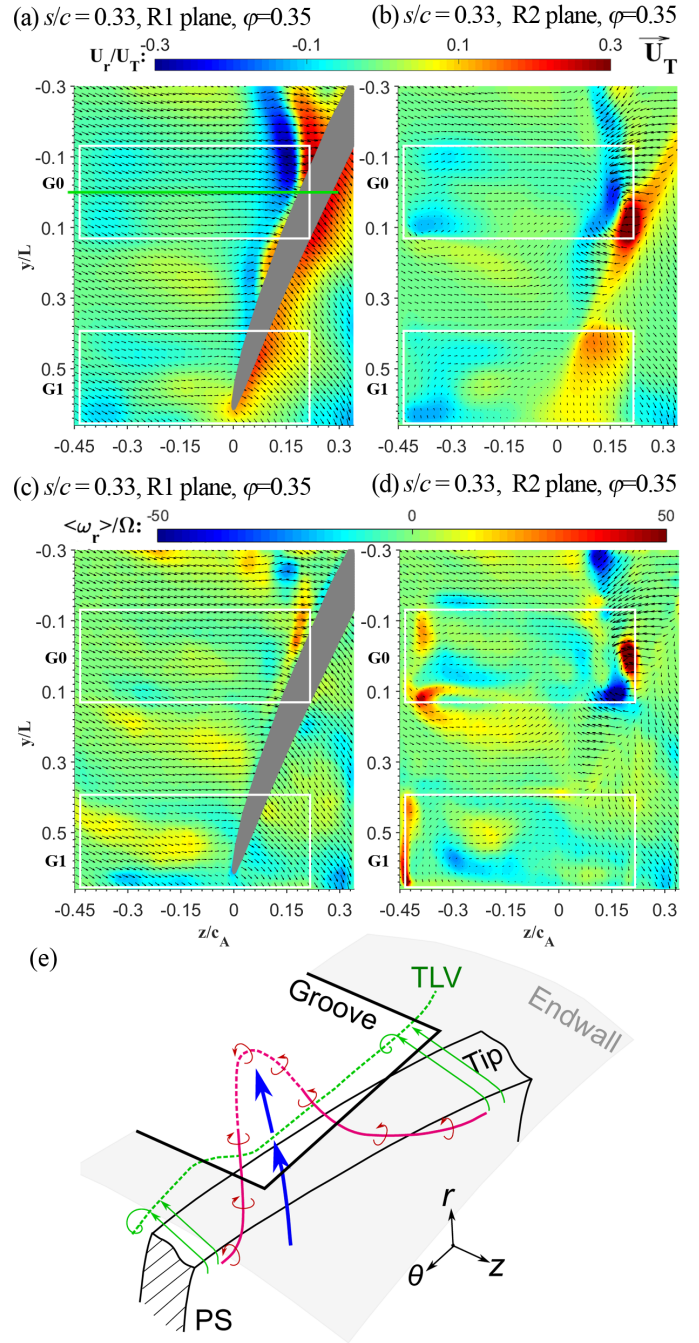
Figure 7: Effect of flow rate on the distributions of $\langle\omega_\theta\rangle/\Omega$ (contour) superimposed on vectors of (U_z, U_r) at s/c=0.44. The flow rate is indicated above each plot. Vectors are diluted by 4:1 in both directions.
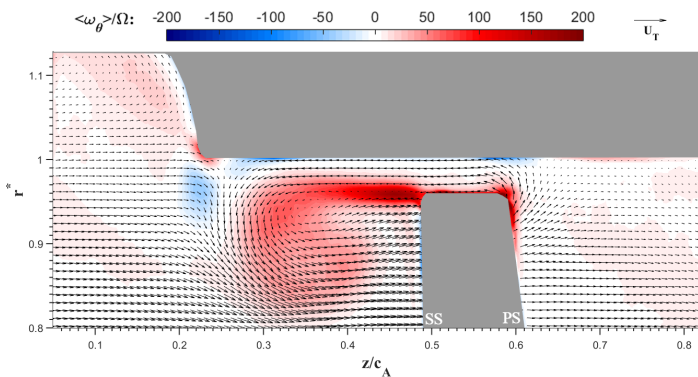
Figure 8: The distributions of $\langle\omega_\theta\rangle/\Omega$ around the blade tip for s/c=0.66 and φ=0.38. Vectors are diluted by 3:1 in both directions.

Figure 9: (a-d) Ensemble-averaged in-plane velocity vectors (nearly U_z, U_θ) superimposed on contours of the radial velocity (top row) and radial vorticity (second row) components at s/c=0.33 and φ=0.35. Left column: r^*=0.96. Right column: r^*=0.98. Vectors are diluted by 4:1 in both directions. (e) A sketch illustrating the vortex-groove interactions.
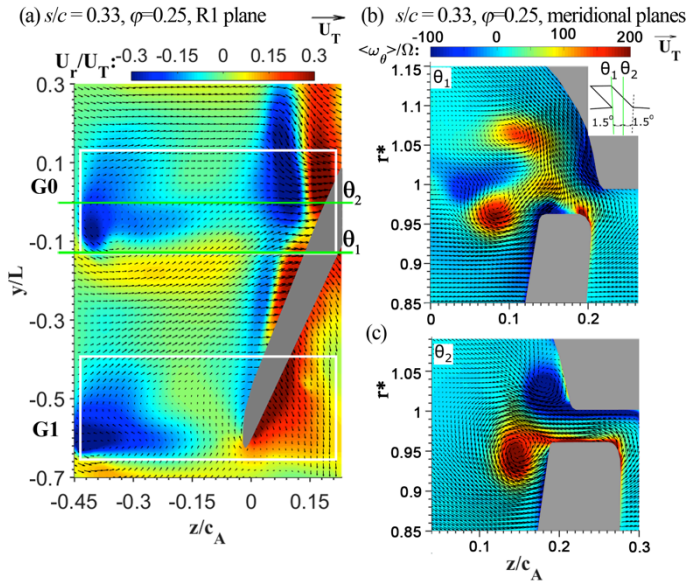
Figure 10: Flow features at $s/c = 0.33$ and $\varphi=0.25$ illustrating the vortex-groove interactions. (a) U_r contours in a radial plane at r^*=0.96. (b and c) $<\omega_\theta>/\Omega$ distributions at two meridional planes.

caused by entrainment into the groove of the PS vorticity by the radial jet. Fig. 9e is a qualitative visual aid aimed at illustrating this process. The PS boundary layer vorticity has positive $<\omega_\theta>$. When this vorticity is pulled into the groove at the corner, it creates counter-rotating vortex filaments that cross the radial plane coinciding with the tip gap (Fig. 9d), but has limited signature in the r^*=0.96 plane (Fig. 9c) except for a mild change in the sign of $<\omega_r>$ on the PS. The fast entrainment of flow originating from the PS is also consistent with the cavitation image in Fig.4a. In fact, there are two possible origins for the positive circumferential vorticity appearing near the PS corner of the blade tip. The first is the PS boundary layer, and the second involved entrainment of upstream parts of the endwall boundary layer by the blade PS, which prior publications refer to as a scraping vortex [29]. Given the present relatively large gap as well as the fact that the elevated PS positive vorticity appears well below the (e.g. Fig. 5), we believe (but cannot verify) that the PS boundary layer is the primary origin of the positive vorticity near the PS corner.

To further understand the impact of entrainment of vortex filaments into the groove caused by the rapid jetting, Fig. 10 provides sample results for $\varphi=0.25$ and s/c=0.33. The U_r distributions at r^*=0.96 and $\varphi=0.25$ (Fig. 10a) shows similar kinks in the TLV trajectory along the blade SS and radial jetting into the grove when the blade PS is aligned with the downstream end of the groove. However, the radial velocity magnitudes are much higher than those measured at $\varphi=0.35$, consistent with the increased blade loading with decreasing flow rate and the results presented in Fig. 7. Figure 10b shows the distributions $<\omega_\theta>$ and (U_z, U_r) in the θ_1 meridional plane, which intersects with the entrance to the groove close to its high θ corner, as illustrated in the insert. This plane is located in

the same area as the high speed radial jet discussed before, enabling us to observe the flow structure in this region. Several phenomena are evident from Fig. 10b. First, a high-speed jet originating from the blade PS penetrates into the groove. Second, apart from the distinct TLV near the blade SS, another vortex with $<\omega_\theta> >0$ originating from the blade PS is located inside the groove, at the upstream edge of the jet. There is no sign of the positive vortex in the θ_2 plane cutting through the groove center, and the corner is dominated by the corner vortex. These observations along with those seen in Figs. 9a-d are consistent with the illustration presented in Fig. 9e. As part of the PS vorticity is entrained into the groove by the jet, instead of rolling up into the TLV, it alters TLV trajectory, keeping the vortex concentrated near the downstream corner of the groove. Note that the variations in the magnitude of U_r along the blade SS might also be affected by radial variations in the location of the TLV center evident by comparing the radial location of the TLV in Figs. 10b and c. In Figs. 10b the TLV center is located above the r^*=0.96 plane, but at the center of the groove (Fig. 10c) the TLV center nearly coincides with this plane.

The tip flow-groove interactions at s/c=0.55 and φ=0.35 are shown in Fig. 11. Here, the blade SS is located downstream of the G0 groove, as shown also in Figs. 4b and 5c. At r^*=0.96 (Fig. 11a), the TLV signature still has a discontinuity near the high θ corner of the G0 groove. However, in this case, the same area has a strong flow aligned almost perpendicularly to the blade chord. This flow is much weaker in the r^*=0.98 plane (Fig.11b), where TLV signature essentially disappears. Instead, the radial velocity in the downstream corner of the G0 groove shows transition from positive to negative U_r, consistent with the flow induced by the corner separation vortex, as shown in Fig. 5c. Figure 11b also shows the rapid change in the direction of U_z as the tip leakage flow meets the incoming main passage flow, also consistent with the meridional plane data (Fig. 5c). In this phase, both the inflow and outflow from G0 groove are weak. However, consistent with the blade location, there is still strong jetting into the G1 groove in the region where it is exposed to the blade PS, and accordingly, a higher outflow from the upstream end.

The $<\omega_r>$ distributions in Figs. 11c&d show more complicated vortex-groove interactions. First, in Fig. 11c, a positive radial vortex is located in the middle of the G0 groove downstream end. It is bounded on both sides with regions containing negative $<\omega_r>$. The high-speed flow perpendicular to the blade chord is bounded by the positive vortex on one end and a weaker negative vortex on the other. In Fig. 11d, at r^*=0.98, the previously discussed vortex pair observed at s/c=0.33 appears to persist in this phase as well. However, the positive vortex in the middle of the groove might also be related to the negative vorticity layer/line appearing at $y/L<$-0.1. The qualitative illustration in Fig. 11e is an attempt to provide a plausible explanation for these observations. The red vortex line is similar to that observed at s/c=0.33 and discussed before. It is formed initially by the entrainment of the PS vorticity, but due to the low flow into the groove in subsequent phases, it

persists near the downstream corner of the groove. In addition, the blue vortex line in Fig. 11e corresponds to the corner vortex with $<\omega_\theta><0$ resulting from the endwall boundary layer separation. This structure migrates radially outward in the middle of the groove, consistent with Fig. 5c, but has to connect with the endwall boundary layer at a lower r on both sides of the groove. The combined effect of these two 3D structures appears to be consistent with the velocity and vorticity distributions presented in Figs. 11a-d. Both structures contribute to the positive $<\omega_r>$ in the middle of the groove and the negative $<\omega_r>$ on both sides of the groove. However, one should keep in mind that the proposed plausible illustration in Fig. 11e has to be proven either by volumetric three-dimensional velocity measurements using e.g. tomographic PIV, or by systematic measurements in a series of closely spaced parallel planes.

Samples characterizing the interactions of the tip flow with the groove at φ=0.38 and s/c=0.55 are presented in Fig. 12. Except for differences in magnitudes and slight shift in locations, the depicted flow structure is similar qualitatively to that recorded at φ=0.35 (Figs. 11a&b). The TLV discontinuity is evident in Fig. 12a, where the downstream shift in the location of the TLV center is consistent with Fig. 7c. The weaker signature of the corner vortex as well as the flow jetting into the G1 groove can be seen in Fig. 12b. On the upstream end, Fig. 12b shows that there is a radial outflow from the corners/edges of the grooves, and a weak inflow in the middle of the grooves. The magnitude of this outflow is weaker and that of the inflow is stronger than those at φ=0.35 (Fig. 11b).

Changes in flow angle and blade loading

Figures 13a and b compare the distributions of flow angle in the rotor reference frame at φ=0.35 without (Fig. 13a) and with (Fig. 13b) ACGs in a meridional plane located upstream of the blade LE (s/c=-0.11). For convenience, the location of the blade LE, which is about to enter the field of view is marked by dashed lines. As is evident, in the tip region, the grooves increase the flow angle close to the blade LE by a maximum of 7°. This increase diminishes with decreasing radial location, and is hardly noticed at r^*<0.84, indicating that interactions with groove only affect less than 16% of the blade span. A radial view of the flow angle at r^*=0.96 under the same conditions is provided in Fig. 13c. As is evident, as the blade tip LE travels across the grooves, it experiences peak to peak periodic fluctuations in flow angle of around 5°. For comparison purposes, Fig. 13d demonstrates the periodic variations in flow angles at φ=0.25, which is discussed in [1]. Here, the faster outflow from the groove increases the peak-to-peak variations in flow angle to 10°. The radial extent of these variations is also higher at φ=0.25, consistent with Figs. 7a and b. These observations confirm that the influence of the groove on the flow around the blade LE increases with decreasing flow rate.
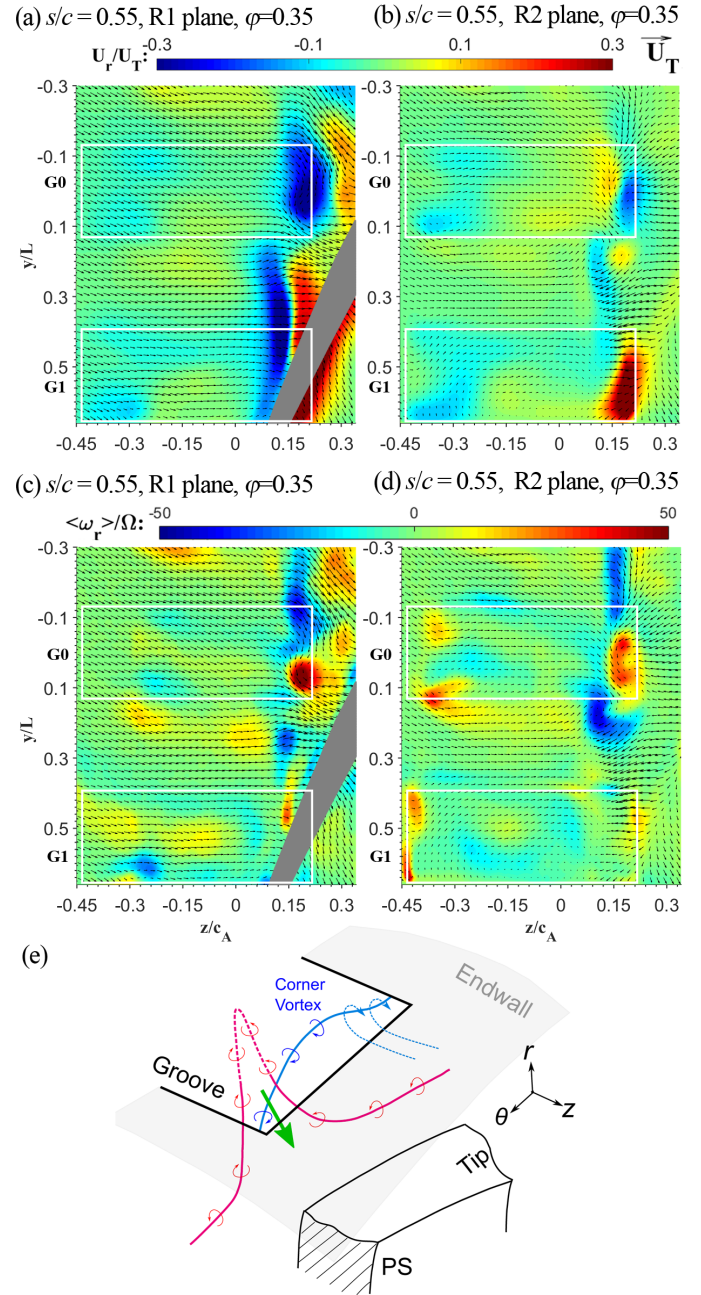
Figure 11: (a-d) Ensemble-averaged in-plane velocity vectors (nearly U_z, U_θ) superimposed on contours of the radial velocity (top row) and radial vorticity (second row) components at s/c=0.55 and φ=0.35. Left column: r^*=0.96; right column: r^*=0.98. (e) A sketch illustrating the vortex-groove interactions.

(a) $s/c = 0.55$, R1 plane, $\varphi=0.38$ (b) $s/c = 0.55$, R2 plane, $\varphi=0.38$
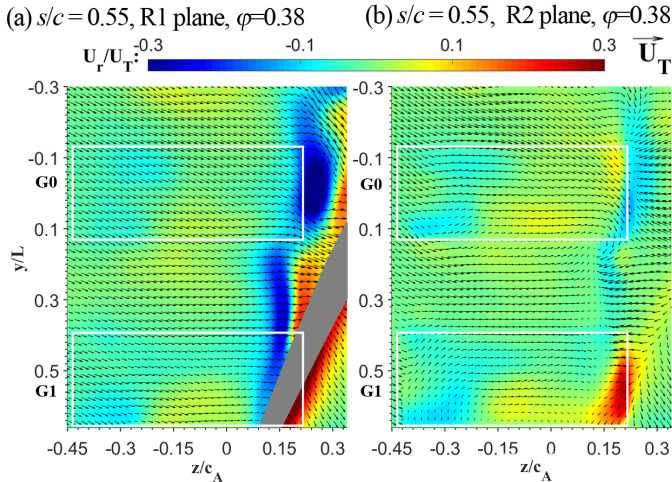
Figure 12: Ensemble-averaged in-plane velocity vectors (nearly U_z, U_θ) at (a) r^*=0.96, and (b) r^*=0.98 superimposed on contours of the radial velocity at s/c=0.55 and φ=0.38.

Figure 14 examines the effects of the ACGs on the magnitudes of positive circulation on the blade SS (Fig. 14a), and the tip leakage flow (Fig. 14b). The circulation is calculated by integrating the circumferential vorticity in the regions that it is positive over the entire SS. Unlike previous studies, we do not attempt to separate between vorticity entrained into the TLV and that located in the shear layer connecting the TLV to the SS tip corner since the boundary between them is fuzzy. The tip leakage flow strength, denoted as U^*_n is obtained by (radially) averaging the velocity across the tip gap in a direction normal to the blade chord in the rotor reference frame. Due to variations in the blade location relative to the groove, at s/c=0.33 the leakage velocity is integrated in a plane coinciding with the downstream corner of the groove. In other phases, the calculation is based on integration along the SS tip corner. As is evident from Fig. 14a, at φ=0.25 and 0.35, the circulation in the grooved endwall is persistently higher than those of the smooth endwall. While the periodic entrainment of the TLV into the groove at φ=0.25 decreases the TLV strength at mid chord [1], at φ=0.35, the circulation keeps on increasing, but at a slower rate at s/c>0.55. This slower growth rate downstream of the groove suggests reduction in blade loading in the aft part of the blade. Hence, in spite of the entrainment of parts of the TLV into the groove, the remaining parts are still stronger than those of the smooth wall. This trend suggests that the groove causes an upstream shift in blade loading. Increasing the flow rate to φ=0.38, reduces the TLV strength at low s/c, but the growth rate does not appear to diminish in the aft parts. Examination of the trends of leakage velocity is another way of evaluating the variations in blade loading since U^*_n is expected to increase with pressure difference across the blade. Figure 14b shows that for φ=0.35 and at s/c=0.33, the grooves increase the tip leakage velocity

significantly, consistent with higher circulation there, and the previously mentioned shift in blade loading towards the leading edge of the blade. This shift is consistent with the higher flow angle (Fig. 13) near the LE. For the smooth endwall, the leakage peaks at s/c=0.44, and decreases slowly further along the blade. Conversely, for the grooved endwall, U^*_n decreases monotonically in our measurement range. This decrease is also consistent with the change in the slope of the circulation at φ=0.35 at mid chord. The profiles of U^*_n at φ=0.38, for which we do not have data without grooves, are similar to those at φ=0.35.

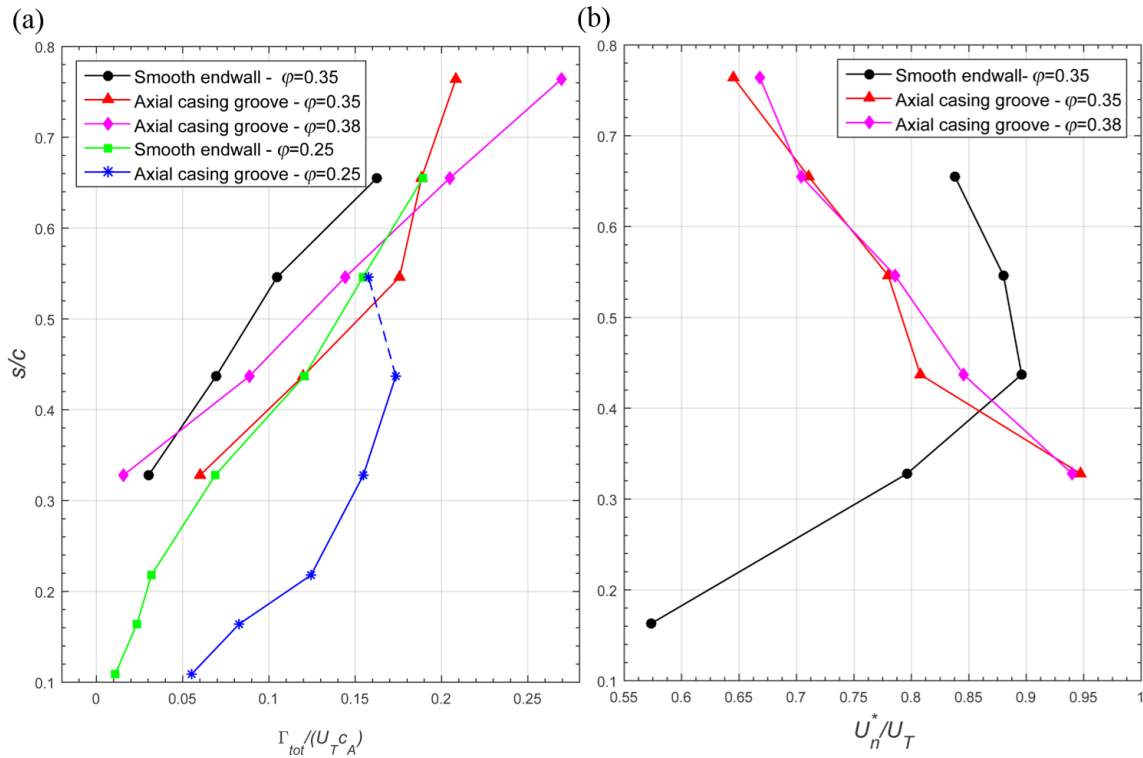*A note on the distribution of turbulence*

Figure 15 provides a sample comparison of turbulent kinetic energy (TKE) distributions with (Fig. 15a) and without (Fig. 15b) casing grooves. The TKE is defined as $k = 0.5(\overline{u'_r u'_r} + \overline{u'_\theta u'_\theta} + \overline{u'_z u'_z})$ and can be used in the present discussion as a statistical measure of flow instabilities. In Fig. 15a, the TKE level is high around the centers of the TLV and corner vortex, as well as in the shear layer connecting the TLV to the SS corner. The area with elevated TKE in the grooved endwall case is much broader than that of the smooth casing, but the peak value near the TLV center and in the shear layer are lower. The wide area with elevated TKE in the PS of the blade in Fig. 15a is associated with remnants of the TLV originating from the previous blade. Similar phenomena have been observed before for the smooth endwall as well [1,22]. Using a significantly different scale, Fig. 15a also shows that the TKE is elevated in the shear layer originating from the upstream end of the groove and separating between the main passage flow and slow circulating flow inside the groove. This elevated turbulence representing loss of mean flow kinetic energy is likely to adversely influence the efficiency of the machine.

SUMMARY AND CONCLUSIONS

Consistent with previous studies [9–11], the axial casing grooves effectively delay the onset of stall at low flow rates, but degrade the performance of the machine around the best efficiency point. SPIV measurements and flow visualizations have been used for investigating the flow mechanisms involved and comparing them to those observed near a smooth endwall. The skewed semicircular, four-per-passage ACGs are based on those described in Müller et al. [2]. They partially overlap with the rotor blade LE, and the rest extend upstream. The present measurements have been performed close to and at the BEP. The complement data obtained under the pre-stall conditions of the untreated rotor [21], and previous measurements at low flow rates using the same grooves [1]. Combined, the extensive experimental database elucidates many of the complicated interactions of the blade tip flow with the grooves.
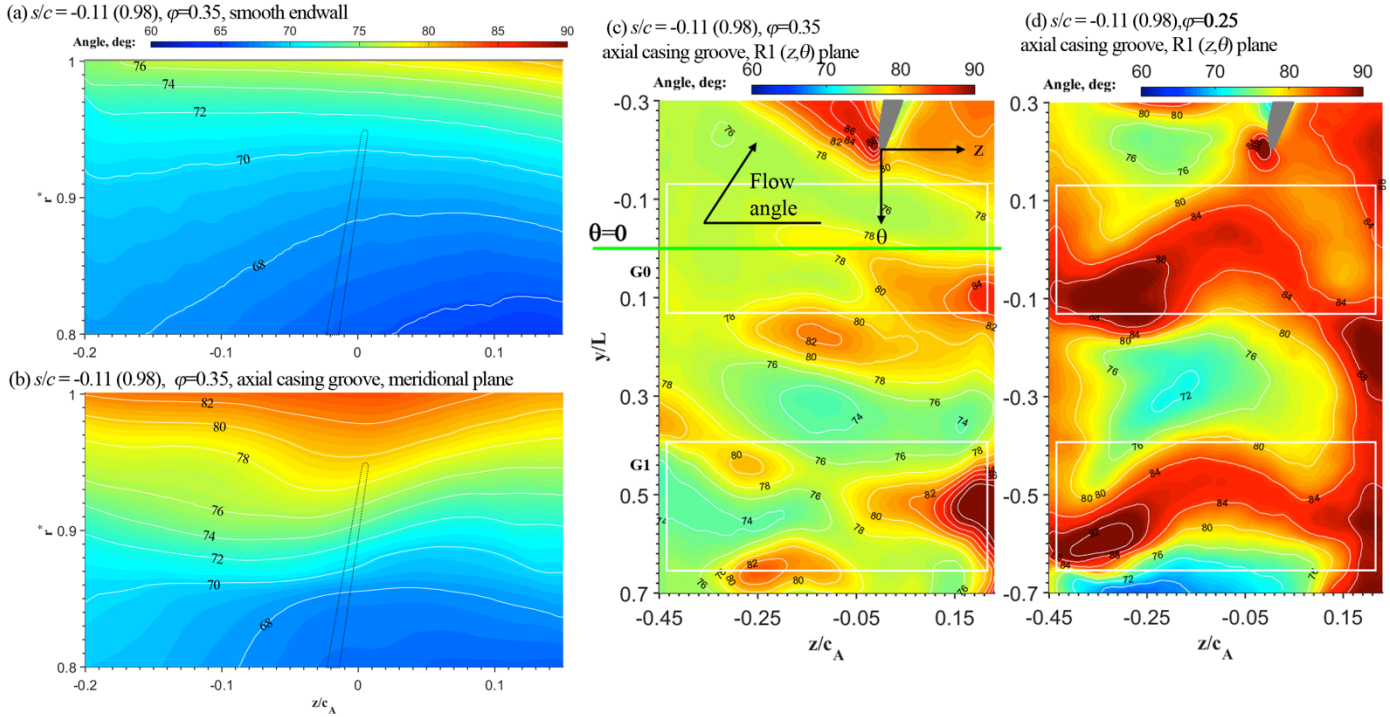
Figure 13: Distributions of relative flow angles in the rotor reference frame at s/c=-0.11 and φ=0.35 in meridional planes (a) without and (b) with casing grooves, and (c) in (z, θ) plane at blade tip with casing grooves. Results from φ=0.25 are shown in (d) for comparison. Dashed lines in (a&b) indicate the location of the blade LE at s/c=0.

Figure 14: Comparisons of (a) total positive circulation at blade SS and (b) tip leakage flow strength normal to the blade chord with and without casing grooves.
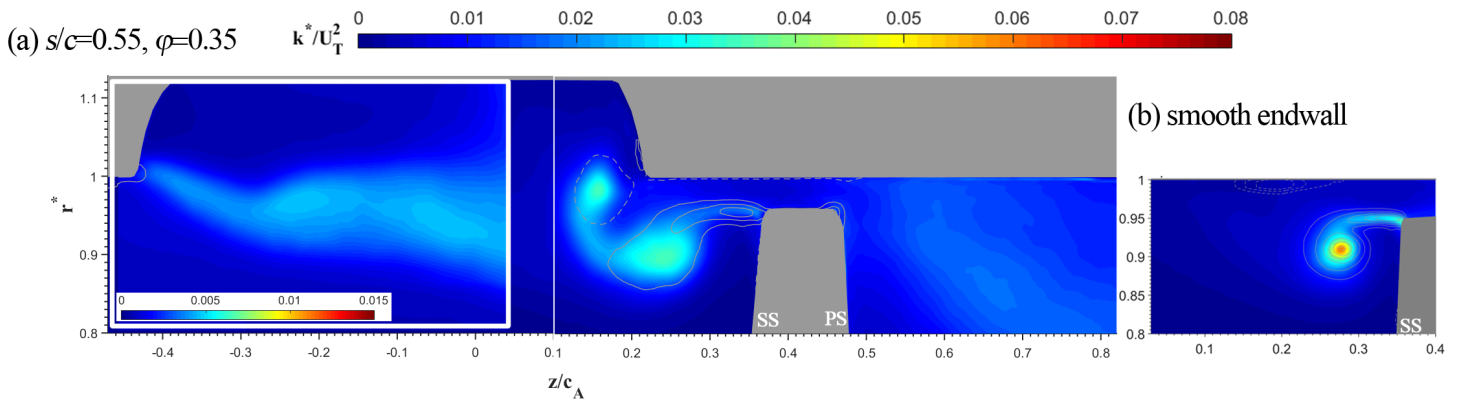
Figure 15: Distribution of turbulent kinetic energy (a) with and (b) without axial casing grooves at s/c=0.55 and φ=0.35. Note the scale for the insert in (a) has a significantly smaller range. Contour lines show the circumferential vorticity.

While it is difficult to summarize all the observed phenomena in a few sentences, several appear to be particularly important. The radial inflow into the groove peaks periodically when the blade PS is aligned with downstream corner of the groove. The resulting rapid radial jet entrains vorticity originating from the PS boundary layer into the groove, preventing it from rolling up into the TLV. This process forms a three-dimensional structure that appears as a counter-rotating pair of radial vortices at the entrance to groove, and causes a kink in the TLV trajectory. During this period, there is a weak outflow from the upstream end of the groove. The inflow into the groove diminishes when its downstream end is exposed to the blade SS. Instead, separation of the endwall boundary layer as the backward leakage flow reaches the downstream corner of the groove generates a large corner vortex, which rotates in the opposite direction of the TLV. At low flow rates, this corner vortex is forced into the groove, and has a limited influence. Conversely, near the BEP, as the PS driven inflow into the groove diminishes, interactions of the corner vortex with the TLV become the dominant flow phenomenon. At φ=0.35, this corner vortex lingers around the downstream corner of the groove, causing fragmentations of the TLV, and generating a broad area with high turbulence level. At φ=0.38, the corner vortex remnants migrate away from the groove together with the TLV, and can be detected even at the blade trailing edge.

During periods of increased inflow, there is also a weak outflow from the upstream end of the groove. However, in other phases, most of the high secondary flows are confined to the downstream corner, and the flow in the rest of the groove is limited to slow circulation with a growing shear layer separating it from the main passage flow. This process persists until the next blade arrives. The grooves also increase and cause periodic variations in the flow angle near the blade tip LE. Accordingly, the magnitudes of circulation shed from the blade tip and leakage flow also increase near the leading edge. These observations might guide potential improvements to the geometry of the grooves that would (e.g.) prevent the lingering effect of the corner vortex at high flow rates.

Finally, the paper concludes with a discussion about possible mechanisms that would cause a reduction in efficiency of the grooved machine at high flow rates. While the flow around the grooved endwall is extremely complex and the present measurements examine only a few sections of the flow domain, the database enables us to identify several of the key phenomena: First, the periodic outflow from the groove increases the blade incidence angle, and appear to shift the blade loading upstream, as confirmed by the increase in leakage velocity and TLV circulation. Such an upstream shift occurs also with decreasing flow rate, which involves also a reduction in efficiency when the machine is operating off its optimized load distribution. Second, the grooves cause generation of a series of secondary flow structures, and consequently increase the area with elevated turbulence in the tip region. In particular, a sizable corner vortex, which remains confined to the groove at low flow rates, is entrained by the TLV into the passage as the inflow into the grooves diminishes with increasing flow rate. Close to the best efficiency point, the corner vortex migrates with the TLV and remains noticeable all the way to the trailing edge. In contrast, the endwall boundary layer negative vorticity remains close to the endwall in the untreated passage. Third, interactions of the TLV with this corner vortex result in a much larger and more broadly distributed TLV circulation, extending it to r*=0.75 (at s/c=0.66), as opposed to r*=0.85 for the smooth endwall at the same location (Figs. 5d&h). Clearly, tip leakage effects propagate deeper into the passage in the grooved endwall at high flow rates. While suction of the TLV reduces its signature in the passage at φ=0.25, the opposite effects occurs around the best efficiency point, when the radial velocity into the groove diminishes.

ACKNOWLEDGMENTS

REFERENCES

[1]   Chen, H., Li, Y., Koley, S. S., Doeller, N., and Katz, J., 2017, "An Experimental Study of Stall Suppression and Associated Changes to the Flow Structures in the Tip Region of an Axial Low Speed Fan Rotor by Axial Casing Grooves," J. Turbomach., **139**(12), p. 121010.

[2]   Müller, M. W., Schiffer, H.-P., Voges, M., and Hah, C., 2011, "Investigation of Passage Flow Features in a Transonic Compressor Rotor," Proceedings of ASME Turbo Expo 2011: Power for Land, Sea and Air, Vancouver, Canada, pp. 1–11.

[3]   Moore, R. D., Kovich, G., and Blade, R. J., 1971, "Effect of Casing Treatment on Overall and Blade Element Performance of a Compressor Rotor," NASA Techincal Note, p. TN D-6538.

[4]   Osborn, W. M., Lewis, G. W. J., and Heidelberg, L. J., 1971, "Effect of Several Porous Casing Treatments on Stall Limit and on Overall Performance of an Axial-Flow Compressor Rotor," NASA Techincal Note, p. TN D-6537.

[5]   Takata, H., and Tsukuda, Y., 1977, "Stall Margin Improvement by Casing Treatment --- Its Mechanism and Effectiveness," J. Eng. Power, **99**(1), pp. 121–133.

[6]   Smith, G. D. J., and Cumpsty, N. A., 1984, "Flow Phenomena in Compressor Casing Treatment," J. Eng. Gas Turbines Power, **106**(3), pp. 532–541.

[7]   Brandstetter, C., Kegalj, M., Wartzek, F., Heinichen, F., and Schiffer, H.-P., 2014, "Stereo PIV Measurement of Flow Structures underneath an Axial-Slot Casing Treatment on a One and a Half Stage Transonic Compressor," 17th International Symposium on Applications of Laser Techniques to Fluid Mechanics, Lisbon, Portugal, pp. 1–18.

[8]   Crook, A. J., Greitzer, E. M., Tan, C. S., and Adamczyk, J. J., 1993, "Numerical Simulation of Compressor Endwall and Casing Treatment Flow Phenomena," J. Turbomach., **115**(3), pp. 501–512.

[9]   Fujita, H., and Takata, H., 1984, "A Study on Configurations of Casing Treatment for Axial Flow Compressors," Bull. JSME, **27**(230), pp. 1675–1681.

[10]   Wilke, I., and Kau, H.-P., 2004, "A Numerical Investigation of the Flow Mechanisms in a High Pressure Compressor Front Stage With Axial Slots," J. Turbomach., **126**(3), pp. 339–349.

[11]   Seitz, P. A., 1999, "Casing Treatment for Axial Flow Compressors," University of Cambridge.

[12]   Beheshti, B. H., Teixeira, J. A., Ivey, P. C., Ghorbanian, K., and Farhanieh, B., 2004, "Parametric Study of Tip Clearance—Casing Treatment on Performance and Stability of a Transonic Axial Compressor," J. Turbomach., **126**(4), pp. 527–535.

[13]   Weichert, S., Day, I., and Freeman, C., 2011, "Self-Regulating Casing Treatment for Axial Compressor Stability Enhancement," ASME 2011 Turbo Expo: Turbine Technical Conference and Exposition, ASME, Vancouver, Canada, pp. 225–237.

[14]   Wu, H., Tan, D., Miorini, R. L., and Katz, J., 2011, "Three-Dimensional Flow Structures and Associated Turbulence in the Tip Region of a Waterjet Pump Rotor Blade," Exp. Fluids, **51**(6), pp. 1721–1737.

[15]   Miorini, R. L., Wu, H., and Katz, J., 2012, "The Internal Structure of the Tip Leakage Vortex Within the Rotor of an Axial Waterjet Pump," J. Turbomach., **134**(3), p. 31018.

[16]   Tan, D., Li, Y., Wilkes, I., Miorini, R., and Katz, J., 2015, "Visualization and Time Resolved PIV Measurements of the Flow in the Tip Region of a Subsonic Compressor Rotor," J. Turbomach., **137**(4), p. 41007.

[17]   Wu, H., Miorini, R. L., and Katz, J., 2011, "Measurements of the Tip Leakage Vortex Structures and Turbulence in the Meridional Plane of an Axial Water-Jet Pump," Exp. Fluids, **50**(4), pp. 989–1003.

[18]   Wu, H., Miorini, R. L., Tan, D., and Katz, J., 2012, "Turbulence Within the Tip-Leakage Vortex of an Axial Waterjet Pump," AIAA J., **50**(11), pp. 2574–2587.

[19]   Tan, D., Li, Y., Chen, H., Wilkes, I., and Katz, J., 2015, "The Three Dimensional Flow Structure and Turbulence in the Tip Region of an Axial Flow Compressor," ASME Turbo Expo 2015: Turbine Technical Conference and Exposition, p. GT2015-43385.

[20]   Li, Y., Chen, H., and Katz, J., 2017, "Measurements and Characterization of Turbulence in the Tip Region of an Axial Compressor Rotor," J. Turbomach., **139**(12), p. 121003.

[21]   Chen, H., Li, Y., Tan, D., and Katz, J., 2017, "Visualizations of Flow Structures in the Rotor Passage of an Axial Compressor at the Onset of Stall," J. Turbomach., **139**(4), p. 41008.

[22]   Li, Y., Chen, H., Tan, D., and Katz, J., 2016, "Effects of Tip Clearance and Operating Conditions on the Flow Structure and Reynolds Stresses within an Axial Compressor Rotor Passage," ASME Turbo Expo, p. GT2016-57050.

[23]   Hah, C., Hathaway, M., and Katz, J., 2014, "Investigation of Unsteady Flow Field in a Low-Speed One and a Half Stage Axial Compressor, Part 2: Effects of Tip Gap Size on the Tip Clearance Flow Structure At Near Stall Operation," ASME Turbo Expo, p. GT2014-27094.

[24]   Bai, K., and Katz, J., 2014, "On the Refractive Index of

Sodium Iodide Solutions for Index Matching in PIV," Exp. Fluids, **55**(4), pp. 1–6.

[25] Wu, H., Miorini, R. L., and Katz, J., 2009, "The Innerstructure and Turbulent Evolution of the Tip Leakage Vortex in An Axial Pump - Part I: Instantaneous Results," Proc. FEDSM2009 ASME 2009 Fluids Eng. Div. Summer Meet., pp. 1–7.

[26] Wieneke, B., 2005, "Stereo-PIV Using Self-Calibration on Particle Images," Exp. Fluids, **39**(2), pp. 267–280.

[27] Roth, G. I., and Katz, J., 2001, "Five Techniques for Increasing the Speed and Accuracy of PIV Interrogation," Meas. Sci. Technol., **12**(3), pp. 238–245.

[28] Westerweel, J., and Scarano, F., 2005, "Universal Outlier Detection for PIV Data," Exp. Fluids, **39**(6), pp. 1096–1100.

[29] Inoue, M., and Kuroumaru, M., 1989, "Structure of Tip Clearance Flow in an Isolated Axial Compressor Rotor," J. Turbomach., **111**(3), p. 250.